PAPER

Structured large-pore foams improve thermal performance of LiMIT-style liquid lithium PFC

To cite this article: M. Szott *et al* 2022 *Nucl. Fusion* **62** 016018

View the article online for updates and enhancements.

Structured large-pore foams improve thermal performance of LiMIT-style liquid lithium PFC

M. Szott[1,*], S. Stemmley[1], C. Moynihan[1], A. de Castro[2] and D.N. Ruzic[1]

[1] University of Illinois, Urbana-Champaign, IL 61801, United States of America
[2] CIEMAT, 28040 Madrid, Spain

E-mail: szott1@illinois.edu

Abstract

As magnetically confined fusion devices improve, the conditions at the walls become increasingly intense. Plasma facing components (PFCs) must withstand these extreme heat and particle loads without damage or degradation. Liquid lithium PFCs are known to be quite resilient, and the presence of lithium also serves to improve plasma properties. The liquid metal infused trench (LiMIT) concept is an open surface liquid lithium PFC design that has been tested extensively at the University of Illinois and in fusion devices around the world. LiMIT utilizes thermoelectric magnetohydrodynamics (TEMHD) to passively drive liquid lithium flow. This work demonstrates an extension of the LiMIT trench geometry to three dimensions. Additively manufactured large pore metallic foams maintain TEMHD drive while drastically improving heat flux handling and resistance to lithium dryout, a phenomenon where locally high TEMHD forces depresses the lithium level and exposes underlying solid structure. COMSOL multiphysics modeling of the system yields insight into the forces at play in dryout development, and shows the 3D structures can eliminate dryout. Low heat proof-of-concept experimental testing of the system matches computational results, and high heat flux electron beam tests more than double the proven operational range of a LiMIT-style PFC, to 6.8 MW m^{-2}, with no indications of dryout or impending damage.

Keywords: liquid lithium, plasma facing component (PFC), thermoelectric magnetohydrodynamics (TEMHD), dryout, high heat flux, COMSOL multiphysics, additive manufacturing

(Some figures may appear in colour only in the online journal)

1. Introduction

Advancements in magnetically confined nuclear fusion plasmas lead to higher plasma density, longer confinement time, and higher plasma temperature. Additionally, future fusion devices will operate under much longer duty cycles, which will serve to drastically increase the total particle and neutron fluence as well as the thermal energy exhausted onto the exposed surfaces surrounding the confined plasma. Plasma facing components (PFCs) must bear the brunt of these extreme

conditions, which can result in a myriad of damage mechanisms on even the most resilient materials. Solid PFC materials routinely exhibit erosion [1–5], thermal damage [6], and fuzz formation [7, 8] in the face of these intense plasma conditions.

One method of mitigating the damage in solid PFCs is through the use of liquid metals, specifically liquid lithium. Liquid lithium PFCs reduce erosion and thermal stress damage, prolonging device lifetime, and have been shown to enhance plasma performance and confinement time, decrease edge recycling, and reduce impurities [9–15]. Flowing open surface liquid metal concepts utilize flowing liquid lithium to provide a constantly refreshing PFC surface and can remove
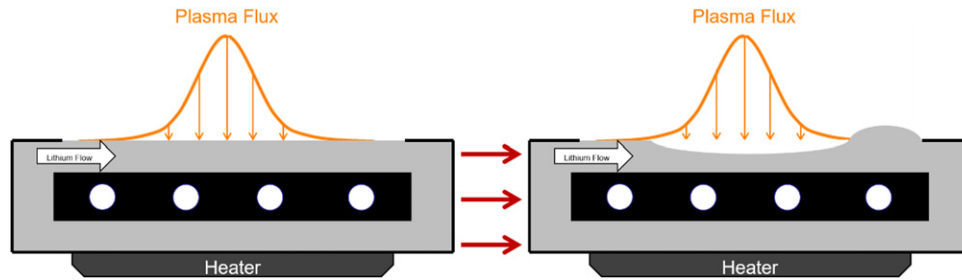
Figure 1. A diagram depicting the development of lithium dryout and pileup in a LiMIT style system under high heat flux impingement. Locally enhanced TEMHD forces drive a depression of the lithium surface, which could expose the solid PFC structure [26].

impurities from the device, though potential concerns include surface stability, wetting control, hydrogen retention, heat flux handling, and scalability.

The liquid metal infused trench (LiMIT) concept pioneered at the University of Illinois harnesses the heat and magnetic fields already present in fusion devices to drive lithium flow via thermoelectric magnetohydrodynamics (TEMHD) [16, 17]. Proof of concept testing at the Center for Plasma Material Interactions [18–21] and larger scale testing in the HT-7 and EAST tokamaks [22–24] and the Magnum PSI linear plasma device [25] have shown sustained flow and improved plasma performance. Continued development of the system has focused on mitigating potential concerns of an open surface liquid metal PFC, including multiphysics system modeling [20, 26], defining stability criteria [27], enhancing ability to control lithium wetting and flow [28–30], and designing systems to recover the hydrogenic fuel species from lithium [31–33]. Current research areas include improving heat flux handling and the design and testing of larger scale systems for use in fusion devices. This work focuses on improvement of the LiMIT system's resilience under high heat loads.

1.1. Heat flux and dryout

Liquid metal systems have additional methods of heat removal in comparison to purely solid PFCs. In order to protect the underlying solid surfaces, the liquid metal components must surpass solid PFC solutions in the ability to survive under high heat loads. Liquid surfaces must stay steady in high plasma impulse and high local heat flux environments. If evaporation, plasma impulse, or divertor/limiter heat stripes thin or eliminate the liquid surface, underlying solids can be directly impacted by the plasma, leading to overheating and damage. In TEMHD-driven systems, the development of high thermal gradients in areas where high localized heat fluxes exist can lead to lithium dryout. The large temperature gradients drive high thermoelectric currents, which translates to TEMHD forces much larger than in the surrounding bulk. As the lithium responds to this higher acceleration, the increased velocity leads to a depression of the lithium surface, which has the potential to expose the underlying solid structure. Additionally, the liquid downstream experiences pileup as the accelerated flow runs into the bulk lithium. This is diagrammed in figure 1.

Dryout occurs when this heat-driven instability in the surface exposes the solid materials beneath the nominal lithium level, which can result in overheating and permanent damage to the solid PFC structure. The thinning lithium layer must also continue absorbing the same heat flux, leading to large increases in temperature and higher lithium evaporation. Several experimental examples of this phenomenon have been observed during extensive testing of the LiMIT system. In 1 MW m^{-2} e-beam heat flux testing at the University of Illinois, 1–1.5 mm dryout is observed directly under the e-beam strike point. The high velocity lithium exiting the e-beam region causes downstream lithium buildup of 2–3 mm. The reduction in cross-sectional area in the highest heat flux region also causes a slight increase in upstream lithium depth. This test lasted approximately 30 s total, with several pulses of the magnetic fields to start and stop lithium flow [26]. Dryout of a similar magnitude resulted in damage to the stainless steel substrate during the first several seconds of a ∼20 s high heat flux test with an average peak heat flux of ∼6 MW m^{-2} [34]. Heat and particle load testing at Magnum PSI displayed thinning of the lithium under the heat spot during several shots, along with buildup and spilling of the lithium downstream. Dryout and buildup magnitudes for these tests are difficult to determine from the infrared imaging. Heat fluxes in these tests reached 3 MW m^{-2}, at which point the module failed due to dryout induced damage [25]. While still performing excellently as a PFC, dryout in LiMIT systems could threaten scalability of the concept to fusion relevant conditions.

This paper demonstrates the improved heat flux handling of an extension of the LiMIT trench concept via 3D modeling and experimental testing. Section 2 describes the experimental and computational methods employed in the study, section 3 explores the results obtained and discusses the scientific implications of the investigations, and finally section 4 outlines the conclusions of the research.

2. Methods

In order to demonstrate effective flow in these systems, computational modeling and experimental testing were undertaken. This section describes the design and manufacturing of the new test modules, as well as the modeling and experimental setup.

2.1. Adjusting the LiMIT trench geometry

The conceptual design behind adapting the LiMIT system to increase resistance to dryout focuses on modifying the
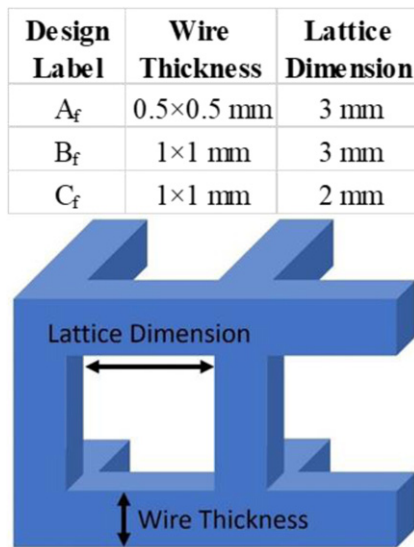
Design Label	Wire Thickness	Lattice Dimension
A_f	0.5×0.5 mm	3 mm
B_f	1×1 mm	3 mm
C_f	1×1 mm	2 mm

Figure 2. Descriptions of the 3D foam designs and the labels referred to throughout this work, with a diagram of the lattice structure included. The designs are cubic lattices with varied square-cross-section structures and on axis spacing, printed via additive manufacturing with 316 stainless steel.

standard trench geometry. The improvements detailed here entail extending the geometry from the standard 1D LiMIT trenches to two and three dimensions of flow channels, resulting in the post TEMHD and foam TEMHD concepts. This work focuses on the 3D large pore foam/mesh TEMHD designs.

The 3D foam TEMHD concept aims to capitalize on the advantages of both LiMIT and capillary porous systems (CPS). Extending the LiMIT concept to three dimensions allows for flow along all three major axes. The design will improve surface stability, both through stronger capillary action helping resupply the surface and through the 3D nature of the foam arresting the characteristic dryout depression. Coupling this with sustained flow solves the passivation, evaporation, and ablation issues with CPS designs. While disordered and ordered foam systems were considered, the disordered foams were developed using a SiC base, resulting in material viability issues with liquid lithium. Hence, this work focuses on ordered large-pore foams. The ordered foam design focuses on improving machinability and heat transfer through a foam, while still utilizing the benefits of the 3D structure. Arrays of wires or mesh are organized in a regimented cubic pattern. This design drastically reduces topside surface material while still providing structure for the surface tension of lithium to maintain surface stability, minimizing the risk of solid structure damage in high heat flux environments. In this case, both wire size and separation can be controlled. Figure 2 lists the geometries studied and the labels with which they will be referenced throughout this work.

Additive manufacturing was used to machine pure 316L stainless steel ordered foams on the millimeter scales described in figure 2. Direct metal laser sintering (DMLS) uses laser heating to selectively fuse a metallic powder bed to build three-dimensional structures layer-by-layer. In order

to reduce initial proof-of-concept test time and cost, a single tri-fold foam plate was designed that incorporates all three ordered foam geometries. Protolabs was chosen to source this plate after considering price, lead time, and confidence in build quality and machinability. The size of the plate required use of the standard resolution 30 μm printer. To avoid the need for supports within the foam features, which would not be removable, the part was built 'corner up' at a 45° angle from each axis. While this method introduces additional risk of warping inherent to additive manufacturing processes, the structure cannot contain additional supports. Tolerance of the standard resolution print is 50 μm in *X* and *Y*, and 100 μm in *Z*, plus 1 μm for each additional millimeter of build. For larger builds, warping due to thermal effects can increase these tolerances. The standard finish procedure for Protolabs's DMLS parts includes heat treatment to minimize warping, removal from platform, support removal, and surface treatment (grit, glass, and spin). The final product is shown in figure 3. The nature of the foam structure precludes any additional surface finishing techniques, so native roughness is seen. The layered sintering process of DMLS creates a grainy surface with R_a value of 5–10 μm, larger than conventional or electrical discharge machining. This can be a concern for effective lithium wetting. Noticeable but infrequent machining defects exist in the foam structure, concentrated predominantly in the smallest 0.5 mm wire section. These do not affect the overall stability or average porosity of the foam sections but present an area for improvement in future designs.

2.2. COMSOL computational modeling setup

COMSOL multiphysics is an extremely powerful, verified tool for finite element analysis and multiphysics simulations [35]. The software package presents an integrated desktop environment into which the user can input relevant physics interfaces contained within large physics modules. Physical parameters can be quickly and directly specified using the predefined interfaces, or the user can enter their own PDEs to be solved. With built-in physics packages for mechanics, heat transfer, electromagnetics, fluids, chemistry, plasma, and more, COMSOL allows for extensive coupling of physics within complex systems. Previous modeling efforts at UIUC have showcased the ability of COMSOL to capture the physics of liquid lithium TEMHD flow and the use the resulting models to inform experimental design [20, 26]. The fully coupled TEMHD model has been validated by past experiments and provides a method of design iteration without physically building and testing each successive attempt. Improvements in computational power allow for larger domains exhibiting lithium flow propensity, including multi-channel flow and recirculation through the bottom side trenches.

The models presented in this work solve the coupled TEMHD flow system in a 3D constrained surface domain as seen in figure 4, where the lithium free surface is modeled as a slip boundary condition. Material properties of the stainless steel and lithium are given in table 1. For simplicity, values are assumed constant over the temperature ranges studied, and are
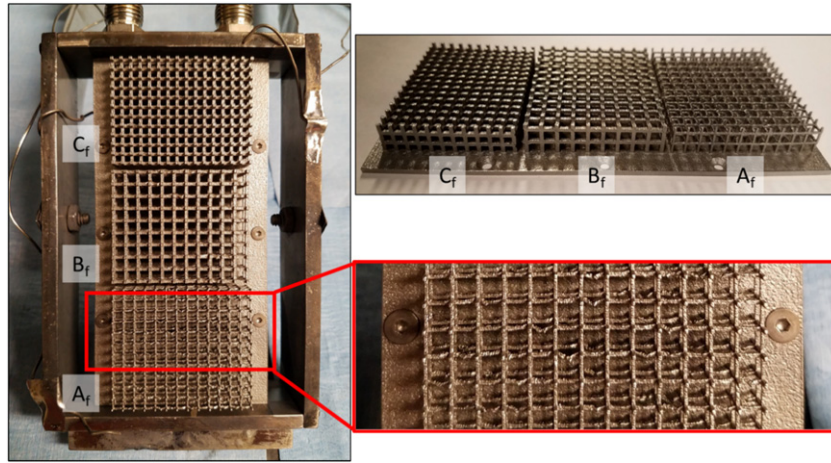
Figure 3. Left: tri-fold foam plate installed in the base module. Top right: side view of the tri-fold foam plate. Bottom right: close-up view of the case A_f foam displaying machining defects.

chosen at an average operating temperature of approximately 573 K (300 °C). Domain adjustments had to be made to rein in spurious currents by ensuring the main flow channels in Y were bounded on either side in X by solid structure. Therefore, the thickness of the domains in X varies from 9 to 11 mm. In order to grasp the 3D nature of the foam, two full layers of each structure type were included in Z, with an additional set of posts at the top. Foregoing the topmost XY layer was done to maximize the amount of lithium flow along the top surface while still providing a solid anchor for surface stability. These adjustments result in topside domain thicknesses ranging from 8 to 11 mm.

TEMHD relies on three main physics interfaces to develop and drive the lithium flow: heat transfer in fluids (HT), electric currents, and laminar flow (LF). The basis of TEMHD flow is the thermal gradients present in the system, so the HT interface solves the energy balance equation, accounting for all sources and sinks of heat

$$\rho C_p \frac{\partial T}{\partial t} + \rho C_p \boldsymbol{u} \cdot \nabla T + \nabla \cdot (-k \nabla T) = Q.$$

Here ρ is the material density, C_p is the heat capacity at constant pressure of the material, T is the temperature, t is time, $\boldsymbol{u}$ is the velocity vector, k is the thermal conductivity of the material, and Q is the net heat source to the system. While the default setup assumes a fluid domain everywhere, heat transfer in solids is easily included in a domain physics node. The initial temperature throughout the domain is set to 573 K (300 °C) in order to match standard experimental conditions. Bottom side heating of the system is introduced via a 17 kW m^{-2} heat flux on the bottommost surface of the domain, which accounts for cartridge heater power and radiated heat flux at experimental temperatures. Topside heating, included when modeling high heat flux conditions, is also introduced as a boundary heat flux node, general inward heat flux type boundary condition on the top surfaces of the domain. To mimic the shape of a heat stripe from a divertor or e-beam, the heat flux is added as a

Gaussian profile with the form

$$q = q_{max} \exp\left(\frac{-\left(y - y_{centerpoint}\right)^2}{\mathrm{Stdev}^2}\right) \left[\mathrm{W\ m^{-2}}\right].$$

Here q_{max} is the maximum value of the curve, $y_{centerpoint}$ is the point along the length of the topside where the peak is centered, and Stdev is the standard deviation of the Gaussian distribution. For this domain, the heat stripe is centered at a $y_{centerpoint}$ of 3 cm, with a standard deviation of 5 mm and an initial q_{max} of 1×10^6 W m^{-2}. Cooling is included as a convective heat flux boundary condition on the cylindrical cutouts that represent the experimental cooling lines. The convective heat flux is given by $q = h(T_{ext} - T)$ where the heat transfer coefficient h is 500 W m^{-2} K^{-1} and external temperature T_{ext} is room temperature, 293 K. The heat transfer coefficient is based off of generic values for forced gas convection and matches previous simulation work for comparison [20].

The EC interface in the COMSOL AC/DC module solves for electric potentials and resultant currents in the domain and derives the next step in computationally modeling TEMHD-driven flow—the thermoelectric current. The interface solves a current conservation equation based on Ohm's law. The set of governing equations is as follows

$$\nabla \cdot \boldsymbol{J} = Q_j,$$

$$\boldsymbol{J} = \sigma \boldsymbol{E} + \frac{\partial \boldsymbol{D}}{\partial t} + \boldsymbol{J}_e,$$

$$\boldsymbol{E} = -\nabla V.$$

Here $\boldsymbol{J}$ is the current density vector, Q_j is the net current source, σ is the electrical conductivity of the material, $\boldsymbol{E}$ is the electric field, $\boldsymbol{D}$ is the electric displacement or electric flux density, t is time, is any external current density vector, and V is the dependent variable electric potential. A ground boundary condition is added on the bottom surface of the domain, as any flowing system will remain grounded in operation. For the TEMHD system, it is assumed that the electric field and displacement
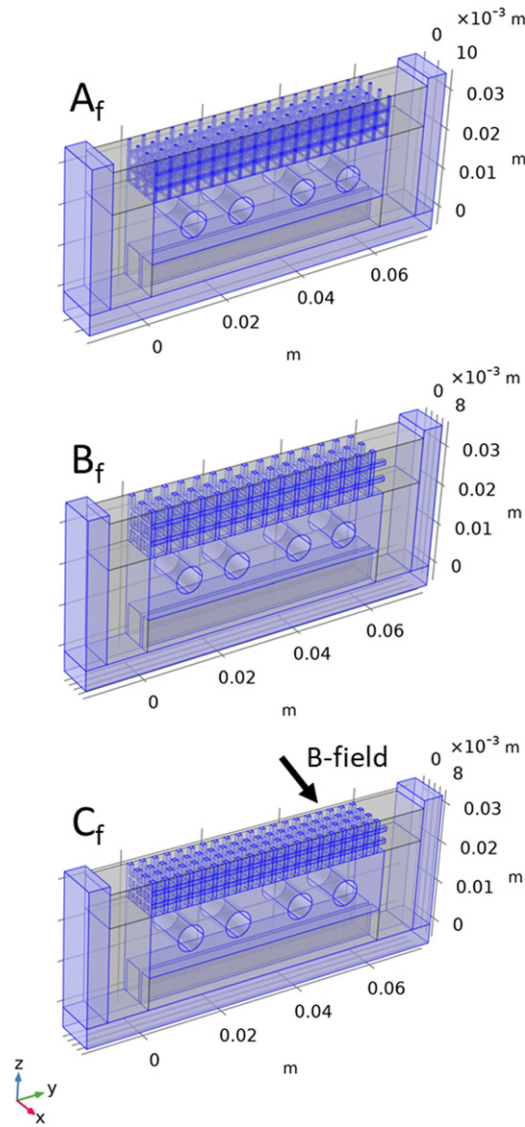
Figure 4. COMSOL modeling domains for the three foam geometries. The solid stainless steel substrate is highlighted in blue, while the lithium domains are gray. The applied magnetic field is in the *x* direction.

Table 1. Relevant material properties of stainless steel and liquid lithium, as included in COMSOL multiphysics modeling.

	Stainless steel	Lithium
Thermal conductivity (W m^{-1} K^{-1})	16	45
Heat capacity (J kg^{-1} K^{-1})	500	4349
Electrical conductivity (S m^{-1})	1.3×10^6	3.6×10^6
Density (kg m^{-3})	7900	508
Dynamic viscosity (Pa s)	N/A	5.03×10^{-4}
Seebeck coefficient relative to stainless steel (V K^{-1})	0	2.5×10^{-5}

allow for effective simulation on relatively short timescales, it is assumed that flow is laminar. For a vast majority of conditions and locations in the domain, the Reynolds number stays under 3000. In the large recirculation channels, the velocity reduction keeps flow laminar. In the high heat regions of the foam structures that exhibit the fastest velocities, the flow will be transitioning to a turbulent scenario, but most conditions remain in a laminar regime. The LF interface solves the Navier–Stokes continuity and momentum equations to find the pressure and velocity field of the liquid [35]. Assuming incompressibility, these equations become

$$\rho \nabla \cdot \boldsymbol{u} = 0,$$

$$\rho \frac{\partial \boldsymbol{u}}{\partial t} + \rho (\boldsymbol{u} \cdot \nabla) \boldsymbol{u} = \nabla \cdot \left[-p\boldsymbol{I} + \mu \left(\nabla \boldsymbol{u} + (\nabla \boldsymbol{u})^{\mathrm{T}} \right) \right] + \boldsymbol{F},$$

where ρ is the density, $\boldsymbol{u}$ is the velocity vector, p is the pressure, $\boldsymbol{I}$ is the identity matrix, μ is the dynamic viscosity, and $\boldsymbol{F}$ is the force vector. By default, the walls are a no slip boundary condition. To aid stability of the pressure calculation, which includes gravity and therefore 'lithistatic' pressure, a 'pressure point constraint' point physics node is added at a corner of the top lithium surface, where there should not be much change in pressure. The pressure reference point for the LF module is set to the same point for consistency. The top lithium surface is modeled as a slip boundary condition to mimic the open surface. The driving TEMHD force is a Lorentz force arising from the thermoelectric current, captured in a domain volume force as follows

$$F_x = 0,$$

$$F_y = j_z B_0,$$

$$F_z = -j_y B_0.$$

The quality of a simulation result is highly dependent on the mesh used to segment the domain. The simulations are time dependent to show the transient development of flow in these new geometries, so minimizing mesh size while maintaining element quality is important for getting results on reasonable time scales. The COMSOL mesh solver was used to mesh the domain, and included refinements near corners and small features, as well as boundary layers along the edges of the fluid domain. Convergence studies were performed to optimize mesh size while maintaining solution integrity. With the aid of the UIUC Beckman Institute Visualization Laboratory,
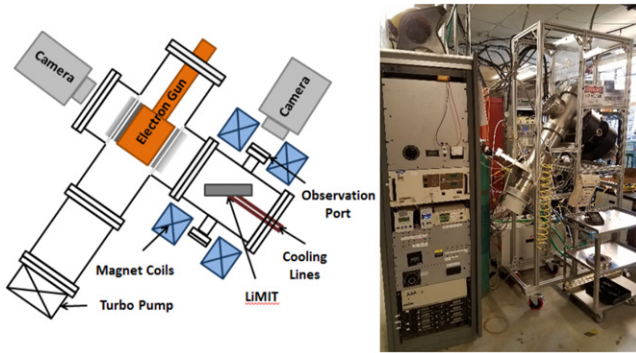
are 0, or very small with respect to the external thermoelectric current. An external current density domain physics node is added to the lithium domains to capture the thermoelectric current, which is split into directional components

$$j_x = \sigma \left(-S \nabla T_x \right),$$

$$j_y = \sigma \left(w B_0 - S \nabla T_y \right),$$

$$j_z = \sigma \left(-v B_0 - S \nabla T_z \right).$$

Here B_0 is the magnitude of the magnetic field, v and w are directional velocity components, S is the Seebeck coefficient, and $\nabla T_{x,y,z}$ are the temperature gradient components.

The COMSOL CFD module has many physics interfaces that are optimized to solve specific types of fluid flow. This setup utilizes the single phase, LF interface to calculate the velocity and pressure fields throughout the fluid domains. To

Figure 5. The SLiDE chamber is a test stand for the LiMIT system, including an e-beam for heating, Helmholtz coils for e-beam focus and TEMHD drive, and module heating and cooling systems.

these simulations were run on two Intel Xeon E5-2670 processors and 128 GB of RAM, with an NVIDIA Quadro K600 graphical accelerator for more effective post processing and visualization. The simulations presented here use a segregated method, with a direct PARDISO solver for every physics interface. It is important to reorder the default segregated system so that the temperature is the first segregated step, followed by electric potential, and then velocity and pressure. Since the segregated solver looks at coupling in the order of the steps, maintaining the order of how TEMHD forces develop proves to be more effective at attaining good convergence and time stepping. Though it varied by model, most simulations were run to several seconds in solution time, RAM usage was typically >15–20 GB, and computation time varied from 30 min to 48 h, depending on the complexity of the geometry and intensity of the heat flux applied.

2.3. Experimental setup

Flow testing of liquid lithium in the standard LiMIT module takes place in the solid/liquid lithium divertor experiment (SLiDE) chamber, shown in figure 5. A summary of pertinent experimental capabilities of the chamber are given here, as well as a description of system improvements that have been made. For a deeper dive into SLiDE systems, refer to [34].

The vacuum chamber is pumped using a roughing pump and turbomechanical pump to reach base pressures on the order of 1×10^{-6} Torr to minimize lithium surface passivation. The system features electromagnetic Helmholtz coils arranged on either side of the flow module installation location to provide the transverse magnetic fields required for TEMHD flow. Proof of concept flow testing is typically run at low magnetic field strengths (200–1000 Gauss) to maximize TEMHD flow speed. The design of the flow module was altered to allow for 60 mm by 120 mm removable topside plates containing novel TEMHD driving geometries to attach to a single base. This reduces cost and time for experimental iteration and improves heat transfer to the metallic structures for enhanced lithium wetting. Diagrams of the module are given in figure 6.
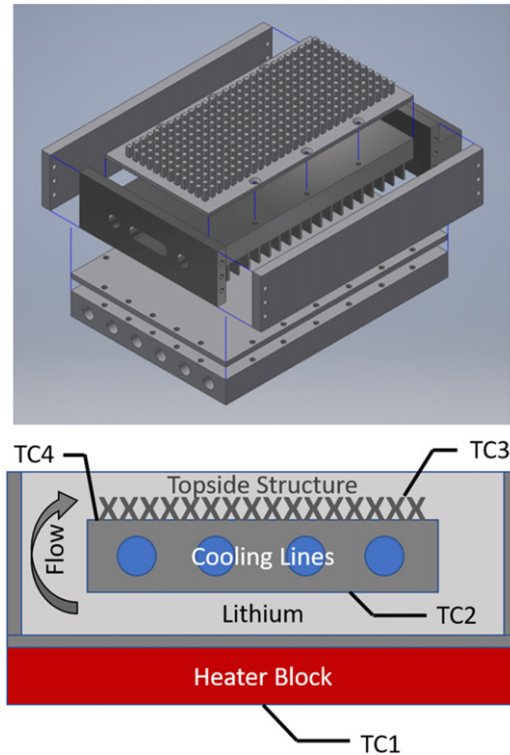

Figure 6. Top—exploded drawing of the modified base module including a test plate geometry as well as side and heater plates. Bottom—diagram of thermocouple placement in the flow module.

Heating and cooling systems in the flow module provide the temperature gradients required to sustain TEMHD drive. Cooling lines snake through the center block of the device, developing temperature gradients on the topside structures and bottom side recirculation channels. Experimental testing was performed with 20 psi forced helium cooling. The heater plate at the bottom of the device provides latent heat through six Watlow E4J30-J6C8H cartridge heaters. These 120 V 200 W cartridge heaters have a 0.5 inch no-heat length at the lead end and braided metal shielding along the leads for overheating and lithium spill protection, respectively. Proof of concept testing of TEMHD flow propensity is carried out with cooling of the latent heating only, allowing for smoother flow conditions to develop. For high heat flux testing simulating fusion device conditions, topside heat is delivered via a linear electron beam. A variable AC transformer (Variac) is used to heat the four thoriated tungsten filaments (Goodfellow 0.15 mm diameter, 99% W, 1% Th) to emission temperatures, and the A.L.E. Systems high voltage power supply provides up to 20 kV of bias for electron acceleration. The e-beam delivers a Gaussian heat flux profile approximately a centimeter wide over a linear distance of approximately 15 cm, with a nominal peak sustainable heat flux of approximately 10 MW m^{-2} and excursions up to 40 MW m^{-2}. For more information on design and operation of the e-beam, refer to [17, 34].

To minimize surface passivation, 75–100 g of lithium is heated in an external reservoir and injected into the flow module via argon backpressure. External components are heated with wrapped fiberglass heating ribbon(s), such as

an Omegalux STH051-040 or similar model. Internal tubing is isolated using Kapton tape and heated with a NiCr NCRR-34-100 resistance heating ribbon. Lithium is heated to approximately 220–250 °C before injection, below the lithium wetting temperature, to mitigate any risk of injector nozzle wetting and leakage due to static lithium pressure in the reservoir. After lithium injection, a fast (to minimize lithium evaporation) temperature excursion to ∼500 °C removes most surface impurities and improves wetting and filling of the solid structures.

Omega K-type thermocouples measure system temperature in four locations on the test module, as shown in figure 6, as well as the reservoir, vacuum feedthrough, and nozzle of the injection system. The thermocouples in the flow module measure the top and bottom of the topside open surface structures, the topside of the recirculation channels, and the base of the heater plate. Temperature data is gathered with the help of a LabJack U6-Pro, along with a temperature tracking VI premade by LabJack and available for download. Temperature measurements of the open surface and the recirculation channels during pulsed B-field operation provide a clear picture of sustained recirculating flow but relating this data to flow speed is challenging.

Current methods of flow visualization and velocity measurement rely on particle image velocimetry (PIV), in which surface particle motion is measured to determine the lithium flow speed. This presents several challenges for quantifying open surface flow characteristics. Impurities on the top surface can block up flow and a passivation layer can hide bulk lithium motion from view. However, some impurities are required to track flow, so effective cleaning of the top surface with temperature excursions could remove the particles required for PIV. Particles floating on the top surface that become entrained in the flow will move at slower speeds than the bulk flow, depending on mass, so PIV gives a reliable but lower bound value of flow velocity. Lithium is also a highly inviscid liquid, so as floating particles are driven in one direction toward the return channels, they can easily spiral around to another part of the flow, creating surface eddy motion. While bulk flow continues recirculating, the surface can quickly develop eddies that mask bulk flow velocities. Pulsing the magnetic fields for short TEMHD-driven tests of ∼5–6 s can reset some particles and allow calming of surface eddies, but also introduces more transient effects. These challenges should be kept in mind, as they are present throughout experimental testing undertaken in this work. Post-test particle tracking is carried out in ImageJ, a powerful open-source, Java-based image processing tool built at the National Institutes of Health and the University of Wisconsin [36]. Videos of the experimental testing are trimmed to highlight each pulse and turned into image series using the open-source image processing tool FFmpeg [37]. The image series of each pulse is imported into ImageJ and the cell counter plugin allows frame-by-frame position measurements of many different particle tracks. A reference point is identified to eliminate motion of the camera or module during the pulse. Particle positions are output from ImageJ and analyzed with Python.
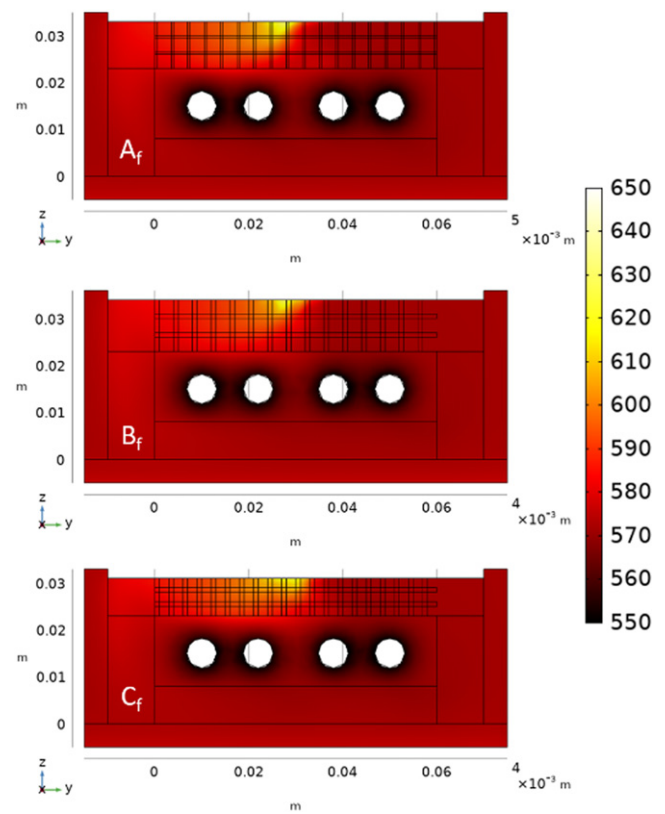

Figure 7. Side view slice of the temperature profile in all foam geometries. Color bar gives temperature in K. The effect of the centered topside heat flux and subsequent flow of hot accelerated lithium is visible.

3. Results and discussion

3.1. Numerical modeling

To test the TEMHD flow potential and dryout mitigation of the proposed ordered foam designs, numerical modeling was undertaken during development of the experimental tri-fold plate. The test conditions are chosen to correspond to high heat flux e-beam testing in SLiDE and are comparable to heat flux values present in large-scale fusion devices. Snapshots of the time dependent simulations are representative samples utilizing a centered Gaussian topside heat flux with 1 MW m^{-2} peak, bottom surface heating of 17 kW m^{-2}, a *B*-field of 0.05 T to maximize flow rates, and convective cooling with 500 W m^{-2} K^{-1} heat transfer coefficient.

The deposition of heat from the topside heat stripe is removed via both conduction and convection. The thermal conductivity of the lithium allows rapid dissipation of heat down to the stainless-steel baseplate, and TEMHD convection rapidly begins to remove heat downstream. The hot lithium circulates into the underside channels, where it is cooled. In the 1 MW m^{-2} case in figure 7, all foam geometries limit temperature rise to below 650 °C. These simulations present a conservative case for heat transfer, as the solid substrate is stainless steel, notorious for its low thermal conductivity. Additionally, the maximum value is reported for the entire topside surface, and therefore always resides within the stainless steel domain.
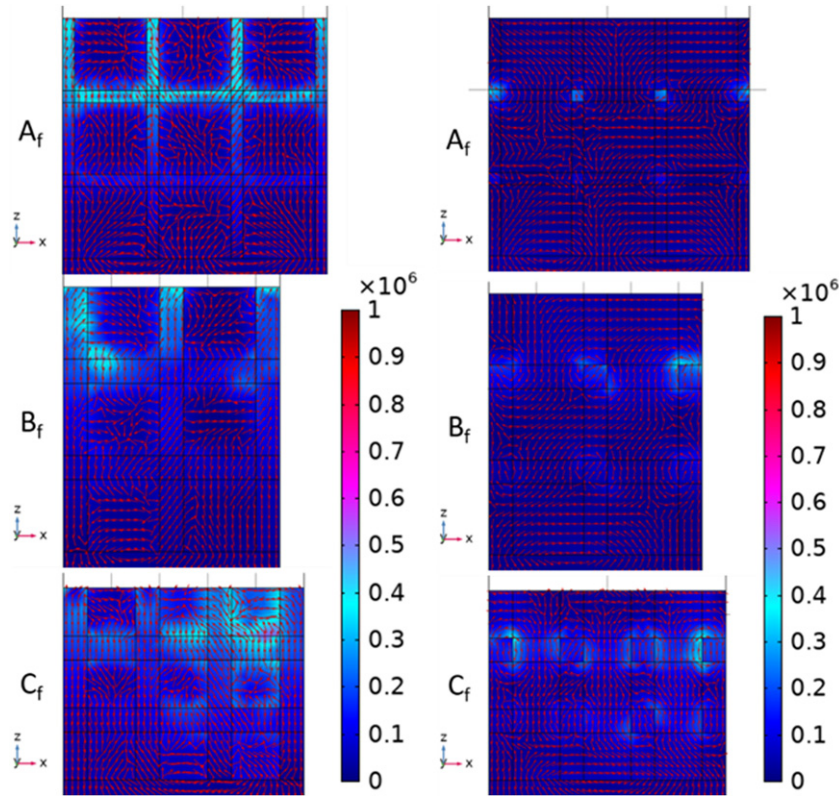
Figure 8. Left: current density plot in an *XZ* slice through a set of *Z*-directed structures near the peak of the topside heat flux, showing larger variability in these flow channels. Right: current density plot in an *XZ* slice in the gap between sets of Z-directed structures near the peak of the topside heat flux, showing more uniform current density development. The color bar shows current density in A m^{-2}. The arrows follow *XZ* current direction.

In experiments, lithium wicking or slight lithium overfill will cover the solid structures with a thin layer of lithium, reducing the maximum temperature.

The temperature gradients from the flow of heat through the system lead to the development of thermoelectric currents, as the liquid and solid materials have different Seebeck coefficients, and therefore have a relative thermopower. The 3D nature of the foam and the small dimensions of the solid structure in relation to the liquid domain leads to development of TEMHD currents unlike those expected in a trench system. In a standard LiMIT trench, the parallel plate arrangement creates a smooth current circulation that travels up through the solid trenches and down through the lithium. In the case of the foams, a variable current flow develops. In between the vertical segments of the ordered structure, the main flow channels do not display an organized directional current. The presence of the horizontal segments in *X* further disrupts the standard current flow. The ordered foams have continual structure along *Y*, and it is here in the 'gaps' between the vertical elements that a more uniform current profile develops, as seen in figure 8. The *Y*-directed foam elements develop a strong current circulation that is predominantly in the −*Z* direction. This TEMHD driving force provides the basis for the directional motion throughout the topside foam domain. Furthermore, the strongest regions of this current are in line with the *X*-directed structures that create the 3D layers along

with the continued structures in *Y*. This means the acceleration in this region will be split by these structures and contribute to effective flow mixing in vertical directions. On average, reduced current peaking in the foam designs in comparison to other TEMHD geometries reduces peak volume forces.

The thermoelectric currents that develop in the foams develop a Lorentz volume force in the presence of the +*X* magnetic field to drive TEMHD flow in the fluid domain. Unique to the 3D foam structures, the main driving force is concentrated along the *Y*-directed structures of the ordered foam. The forces are most extensive in case C_f due to the larger structure-to-flow area, while in the case A_f foam the volume force is difficult to distinguish. For all designs, the volume force magnitude peaks around 5×10^4 N m^{-3}, while average volume forces vary by design between 75 and 400 N m^{-3}. These driving forces result in sustained, recirculating TEMHD flow throughout the domain, a representative snapshot of which is displayed in figure 9. The influence of the cooling channels is evident by the 3 s mark in the simulation, especially in the recirculation channel flow. The apparent reduction in recirculation velocity in case B_f is due to differences in domain sizing leading to the slice sitting close to the channel edge where velocity goes to 0. Due to the 3D nature of the foam structure, the designs have a highly reduced hallmark of dryout, which is typically seen in models as a sustained high velocity lithium profile that drops below the surface of the domain. Here, there is some indication
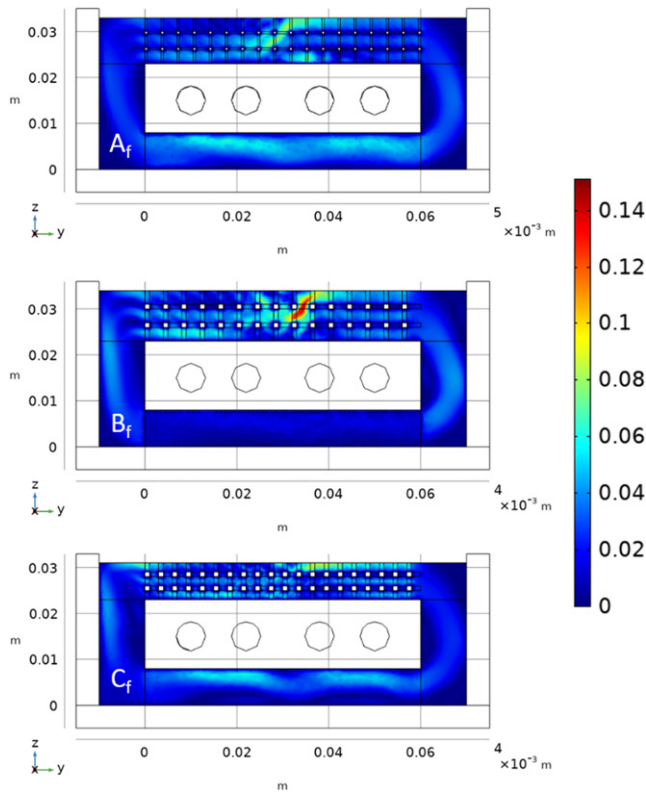
Figure 9. Velocity profile at 3 s of simulation time, showing strong lithium circulation. The color bar gives velocity magnitude in m s^{-1}. In fixed-surface modeling, the characteristic dryout depression is depicted as a high velocity segment of flow that drops from the top surface under the central heat stripe. While some degree of that is seen in the foam designs, the 3D nature of the structures breaks up the high velocity flow in the module center and does not allow a sustained depression to develop, indicating resistance to dryout.

of a dropping high velocity flow directly under the heat stripe, but the 3D structure of the foam helps to immediately break up the rapidly accelerating flow, slow it down, and disperse it among the layered channels in Z. This is especially evident in cases B_f and C_f, as the 0.5 mm structures of case A_f contribute less stabilizing current against dryout.

Examining the directional components of the TEMHD volume force yields additional insight into the development and mitigation of dryout. The Z-directed volume force responsible for dryout and pileup are plotted in figure 10. While the foam cases do not contain strong dryout indicators in the velocity profile, the profiles do not suggest uninterrupted flow, so an examination of the Z-directed forces is warranted. As the heat stripe impinges on the top surface the temperature gradients in Y develop thermoelectric currents along the same direction. These currents result in volume forces that act downward on the lithium on the upstream side of the heat stripe, causing dryout, and upward on the downstream side of the heat stripe, resulting in pileup. In the foam geometries, the dryout forcing is most pronounced along the vertical components of the ordered structure, at odds with the unique driving forces for the predominant Y-directed flow. The $+Z$ and $-Z$ forces are clustered closer to the central heat stripe in cases B_f and C_f, signifying any dryout forming is quickly

countered by pileup forces. The presence of the horizontal structures helps to diminish the magnitude of the forces in the second and third channels from the top, and these structures also contribute to the Y-directed driving force. Case A_f shows disperse forces in Z like the Y-directed forces in figure 10.

The time dependent characteristics of the average and minimum Y and Z volume forces are given in figure 11 in order to examine the relative significance of the optimal driving forces versus the detrimental dryout forces. In all cases, the average Y volume force present at all times signifies sustained recirculation of flow through the domain. The magnitude of this drive increases from case A_f to case C_f, as expected. The 0.5 mm structures cannot drive flow through the large 3 mm channels as readily as the 1 mm structures of case B_f, and the smaller 2 mm channels of case C_f present the most effective TEMHD drive. In all cases, the average Y-directed force initially grows faster than the dryout force. It should be noted that the average force in Z includes both positive pileup forces and negative dryout forces, so the negative average indicates dryout forcing is stronger than pileup and increases in time. The dryout forces begins to dominate the driving force around 2.5 s in case A_f, around 4.5 s in case B_f, and does not overtake average driving force during the 5 s simulation time of case C_f. Another important comparison to make is in the behavior of the peak forces, which describe the largest magnitudes of TEMHD drive ($-Y$) and dryout ($-Z$). When Z-directed forces dwarf those in the Y direction, as seen in other TEMHD designs such as 1D trench flow, high propensity for dryout exists. Here, the peak Z forces are substantially lower than those seen in earlier designs, and always of very similar magnitude to the Y-directed forces. This indicates a substantially reduced potential for dryout in the foam designs, as the peak dryout forces contribute most to initial disturbance of the surface. Instead of a dominant force downward under the heat stripe, the peak forces push lithium down and out of under the heat stripe with similar magnitudes, and the 3D nature of the foam aids in breaking up this downward motion.

3.2. Proof of concept flow

Proof of concept flow testing proceeded on the tri-fold foam plate with only bottom side heating, forced helium cooling at 20 psi, and a low magnetic field that was varied from 0.02 to 0.07 T (200–700 Gauss). The magnetic fields are pulsed 3 times to visualize startup from a no-flow condition after setting up the temperature gradients by cooling for 10 to 20 s. Each time, the B-field is engaged for 5 to 7 s before the knife switches that allow current to flow are disconnected. Thermocouples monitor the temperature of the module for injection, wetting, and performance metrics. Refer to figure 6 for a diagram of thermocouple placement. Unfortunately, midway through heating the system, the top-of-structure thermocouple began to read erroneously, so that data is omitted here. Figure 12 shows a representative temperature trace over the course of three magnetic field pulses. The magnetic field is on at 0.05 T for the periods marked in gray shading.
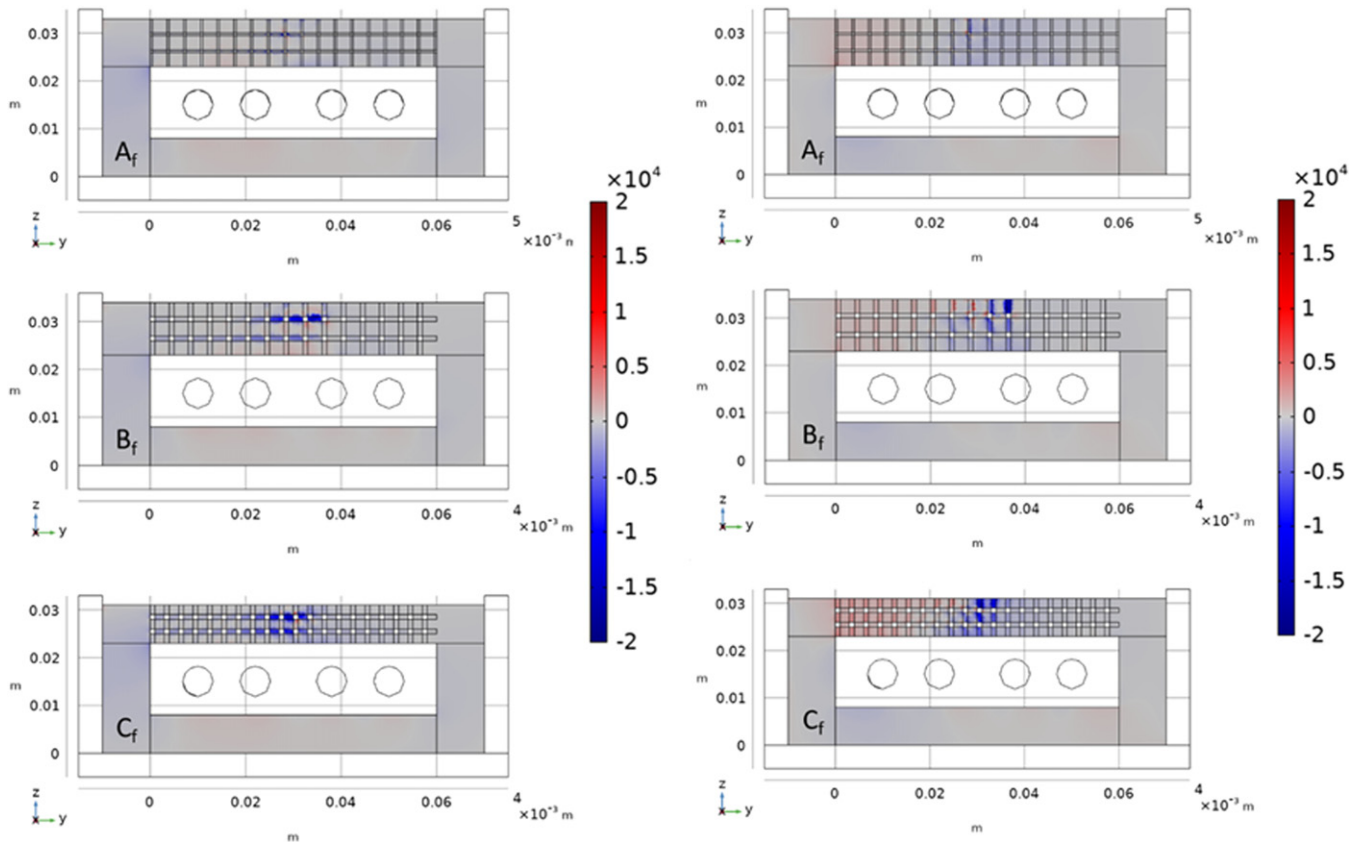
Figure 10. Left—plot of the *Y* component of the volume force providing the primary TEMHD drive. Right—plot of the *Z* component of the volume force providing the impetus for dryout and pileup. The color bars show volume force in N m^{-3}. The relative maximum and average magnitudes of the *Y* and *Z* volume force components provide insight into flow behavior and resistance to dryout. Higher *Y*-directed force in the negative direction indicates better TEMHD drive in B$_f$ and C$_f$, but the larger structures also produce larger *Z*-directed dryout and pileup forces than A$_f$. Ultimately the tighter structure of C$_f$ harnesses the enhanced TEMHD drive forces and mitigates the dryout and pileup forces.
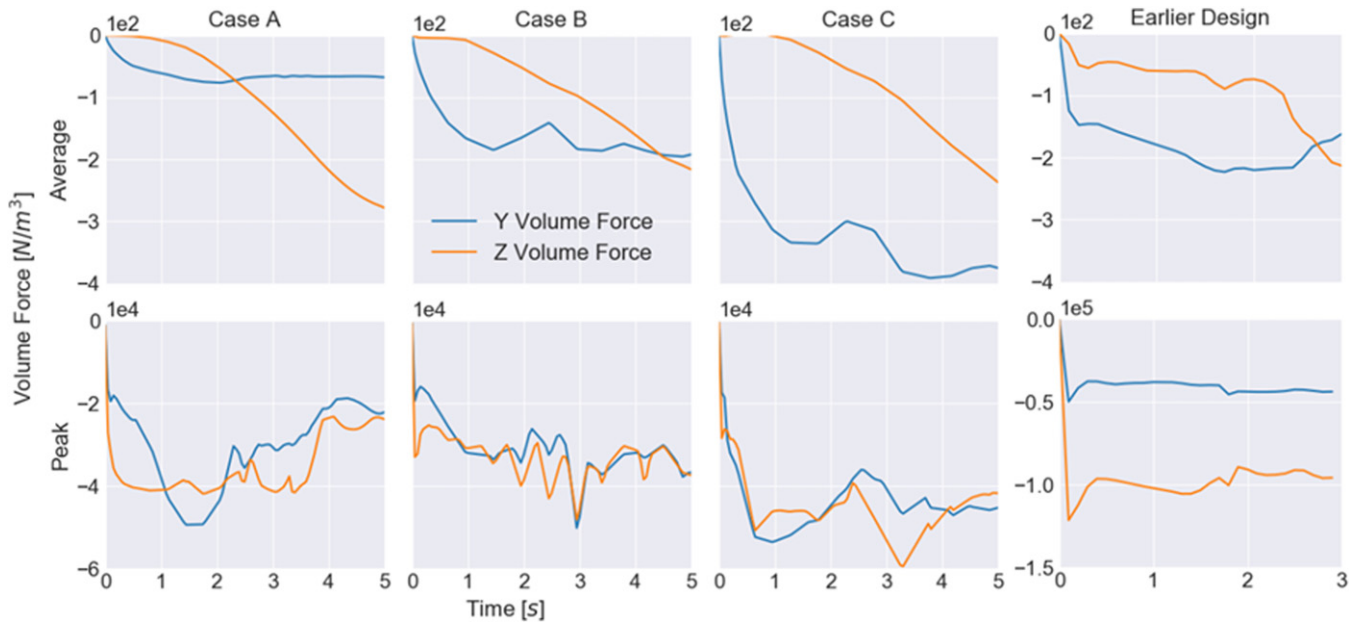

Figure 11. Geometry comparison of minimum and average volume force components over time. The *Y* component of the volume force drives nominal TEMHD flow, while the *Z* component develops dryout. The interplay between these forces, both their extreme and average values, describes the TEMHD flow efficiency and dryout resistance. The right subplots describe an earlier LiMIT-style design that does not perform as well. Note the different scale of the bottom right subplot, showing larger peak *Z* volume forces contributing to enhanced dryout risk.
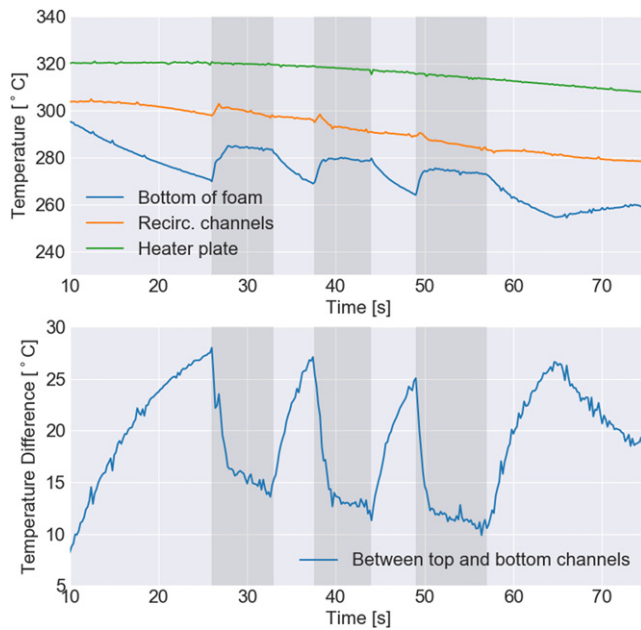
Figure 12. Representative thermocouple response for a set of TEMHD pulses. This proof-of-concept flow test is run with no topside e-beam heating, 20 psi helium cooling, and 0.05 T magnetic field. The shaded bars represent the times the magnetic field is activated, and during these times, the temperature response indicates rapid initiation of sustained TEMHD flow circulation.

Figure 13. Representative COMSOL velocity traces for proof-of-concept flow conditions—no topside heating, 20 psi helium cooling, and 0.05 T magnetic field. Steady flow in all three foam designs is evident in both modeling and experimental testing.

The thermocouple measurements reveal the development of sustained TEMHD flow as soon as the magnetic field is turned on. The bottom of post thermocouple responds to the cooling activation almost immediately and quickly develops a large difference in temperature with respect to the recirculation channels. As the magnets power on, the cooling trend of the topside immediately reverses as flow is driven, mixing along the topside structures occurs, and bulk recirculation exchanges hotter lithium from the recirculation channels with cooler topside lithium. The recirculation channels see a momentary jump slightly delayed from the reversal on the topside and begin cooling at a slightly increased rate due to the lithium circulation. Once the magnetic field is turned off, flow stops, and the original temperature trends quickly reassert themselves as cooling continues.

The COMSOL setup was adapted to run a magnetic field sweep that resembles that of SLiDE. The topside heating is disabled, and each magnetic field value is run for a simulation time of 10 s, to allow steady flow to develop from the thermal gradients created by the cooling lines. The three foam geometries establish smooth velocity profiles circulating around the domain due to the moderating influence of the porous media throughout the topside flow. The unique setup of currents driving flow, as discussed in section 3.1, contributes to this effect (figure 13).

Figure 14 shows the comparison of surface velocity data between the experimental tests and the COMSOL simulations of the three foam cases in SLiDE conditions. The 0.02 T tests did not yield particles to track, but the temperature measurements indicate sustained flow. The average and maximum surface velocities are plotted for the remainder of
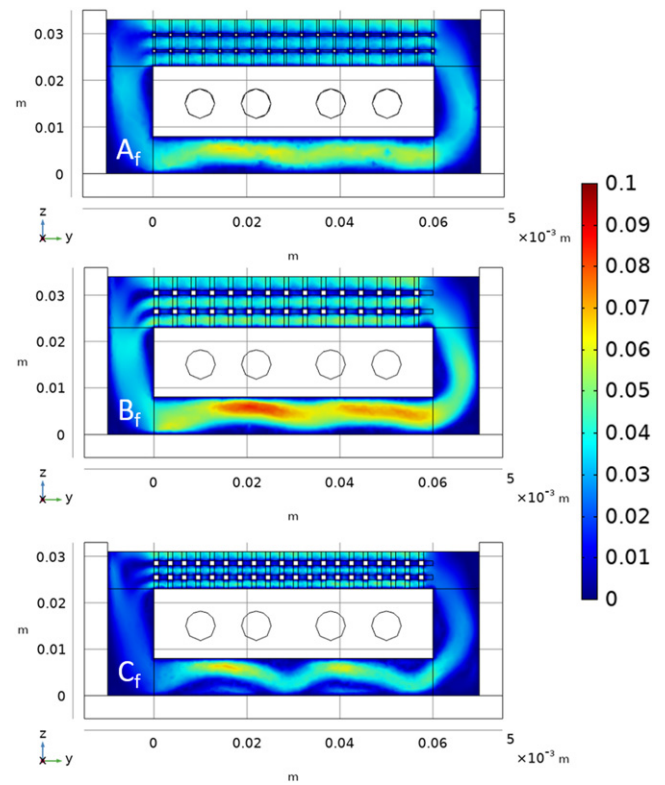
the magnetic field values. In these tests, the particle tracks exhibited appreciable variation, so both the average maximum velocity and overall average velocity of the particles is plotted here with the shading representing one standard deviation.

The experimental values show partial agreement to the velocities predicted by the multiphysics models. The average surface velocities of the modeled foams are all very similar, in the range of 2–3 cm s^{-1}. Experimental values trend above these curves. The average value of the 0.04 T experimental test is outside its expected value. This *B*-field had the least amount trackable particles, all located near the edges of the foam domain, where velocities increased. Maximum values for cases B_f and C_f lie between 9 and 10 cm s^{-1}. The interesting outlier from the models is the maximum velocity curve for case A_f. While the overall velocity profile through the foam largely resembles the other cases, the thin structures proceeding to the topside surface are not able to drive a high maximum topside velocity. Experimental maximum velocities showcase a much larger standard deviation but align quite well with the expected maximum values of cases B_f and C_f, which is expected due to the majority of particles being identified in case B_f.

It is important to mention some of the developments in the experimental flow profiles that affect these velocity values. During the proof-of-concept tests, the effects of cases A_f and C_f were observable indirectly, through the establishment of distinct flow regions. This highlights the downside
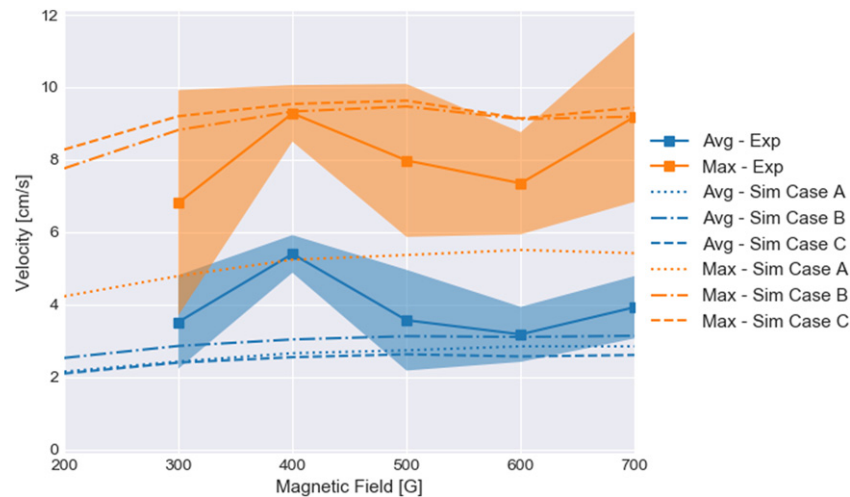
Figure 14. Comparison of proof-of-concept experimental velocity values to a SLiDE-relevant COMSOL magnetic field sweep. Experimental values are given for the tri-fold foam plate as a whole. Limitations in particle velocimetry in the foam designs (see section 2.3) led to most tracked particles traveling through case B_f.

to the development of a single test plate containing multiple geometries and exhibiting differing TEMHD flow speeds. As mentioned in other parts of this work, surface PIV is quite difficult to relate to bulk flow, especially in a highly inviscid liquid, such as lithium. Impurities float on the surface and cannot sink and recirculate with the bulk flow, with the rare exception of extreme heat flux conditions. The fact that fewer particles moved through the domain in the low B-field cases is not included. The error in the experimental curve only accounts for the standard deviation of tracked particles. For pulses with few trackable particles, these particles tend to be well entrained in a primary flow channel and exhibiting higher than expected velocity, resulting in little survey of low velocity areas to correctly account for the average velocity. Additionally, experimental discrepancies in cooling time and B-field pulse length affect the development of the experimental flow profile, adjusting it from the ideal modeled case.

In this experiment, and the majority of TEMHD testing at UIUC, the surface motion is easily decoupled from the bulk recirculating flow. This becomes more apparent with the inclusion of differing topside geometries. Most apparent here is the development of rapid swirling flow in the side channels. The bulk recirculation of the flow, coupled with temperature gradients that develop toward the sides of the module, can drive high speed swirling flow along the side channels. This distinct flow region easily entrains impurity particles that cannot recirculate with the bulk. As seen in figure 14, while the maximum flow speeds of B_f and C_f trend together, case A_f has a reduced surface velocity maximum. In combination with the acceleration in the side channels and the presence of a slight overfill in case A_f, this results in a swirling flow that can reverse portions of the surface velocity over the case A_f foam. The particle velocity slowing in the regions of thinner overfill indicates the action of the underlying bulk attempting to counter the reverse motion, but the decoupled surface motion renders significant portions of the particle tracing unreliable. The data presented above has trimmed the particle motion through these distinct
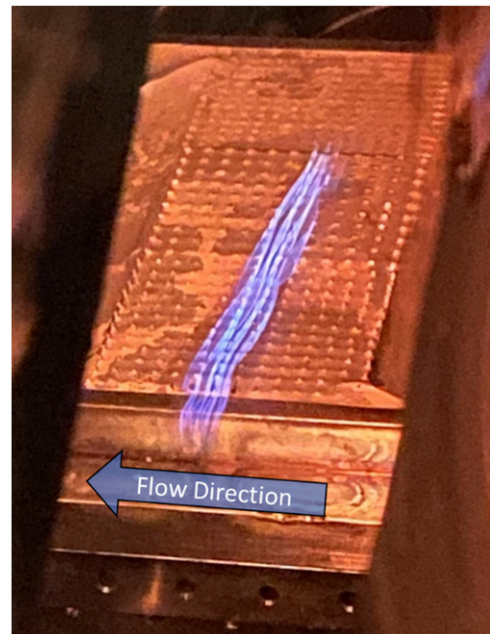

Figure 15. A 10 mA e-beam hitting the surface of the lithium-filled module, with the characteristic blue glow tracing the region of highest emission from the four beam filaments after they are focused in the magnetic field.

flow regions, resulting in more reliable velocity data through the foam. This was most possible for the case B_f region.

There is also noticeable wave motion in the high velocity side channel flow, in which particles can accelerate to well over 20 cm s^{-1}. It is hypothesized that it may be possible to entrain the light impurity particles in the wave motion and accelerate them to speeds faster than the bulk, but this is an avenue for future study. Ultimately, the small scale of the test modules studied at UIUC heightens the magnitude of the effect that these distinct boundary and surface flows can have on the overall surface velocity data. Larger devices, and those with
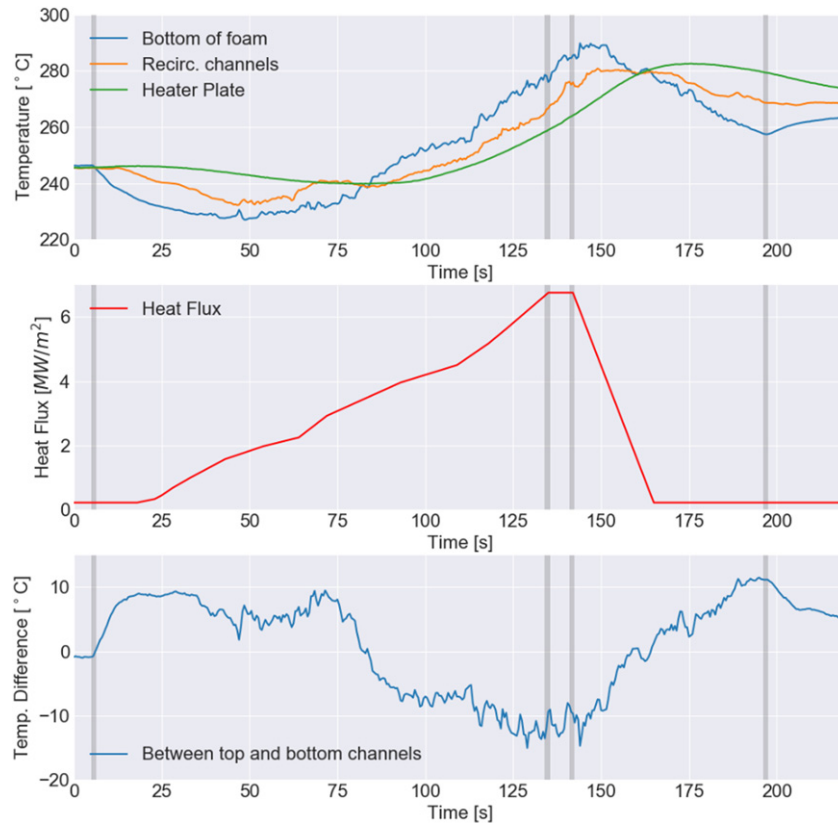
Figure 16. Temperature response over of the tri-fold foam module under high heat flux e-beam heating, with the ramp of beam power included. From left to right, the gray bars mark the start of cooling, start of highest heat flux, end of highest heat flux, and the end of cooling. As flow begins, the recirculation channels are hotter, as in proof-of-concept testing. As topside heat flux increases, the topside channels become warmer. The effective convection of heat via circulating TEMHD flow keeps bulk lithium temperatures under 300 °C, less than a 50 °C temperature increase from initial conditions.

external pumping, will maintain more uniform surface conditions less affected by surface mobility.

3.3. High heat flux testing

The true test of a theoretically improved open surface PFC is whether it can withstand the extraordinarily high fusion-relevant heat fluxes, on the order of 10 MW m^{-2}. At UIUC, the SLiDE chamber comes equipped with a homemade linear e-beam for applying a thin high heat flux region on the surface of the module that mimics a divertor heat stripe in a fusion device. For a brief introduction and visualization of the e-beam placement see the experimental setup in section 2.3, and for a deeper dive into e-beam design, construction, and commissioning, refer to [17]. This e-beam has been utilized for multiple high heat flux tests of the LiMIT device [34]. A typical initial operation condition of 10 kV acceleration voltage and 10 mA beam current is shown on the surface of the filled ordered foam module in figure 15. To achieve beam focus during testing, the magnetic fields must be activated. Changing the current in the Helmholtz coils changes the length and thickness of the beam, which adjusts the ultimate heat flux impinging on the lithium surface.

The temperature plot of the most rigorous heat flux resistance test of the ordered foam plate is presented in figure 16. The top of foam thermocouple registered faulty and inconsistent values, so it is not included here. This test was run with lower bottom side heating of 11 kW m^{-2} to account for e-beam impingement, and 6.5 V, 100 A on the magnetic field power supplies, supplying a focusing field of 0.065 T. At this B-field and 10 kV acceleration voltage, the heat flux is related to the beam current by the following linear relation.

$$q_{peak} \left[\mathrm{MW\ m}^{-2} \right] = 0.0225 I \ [\mathrm{mA}].$$

With q_{peak} as the peak heat flux magnitude and current I. Cooling is started at 5 s, and the beam is in standby mode at 10 kV and 10 mA. At standby, temperature rise of the module in entirety is slow, and cooling is periodically activated to reset to optimal lithium temperatures. The middle subplot shows the peak heat flux value over the duration of the test. Until 2 MW m^{-2}, the 20 psi forced helium cooling lines can remove enough heat to keep the temperature dropping or stable. Past that point, the temperature begins to rise. At 135 s, the peak current of 300 mA was attained, equating to a maximum heat flux of 6.8 MW m^{-2}. This level was held for 5 s before the beam current was quickly lowered. The temperature difference between the top and bottom lithium channels never exceeded 15 °C, indicated sustained bulk flow and mixing throughout the device. The thermocouple at the bottom of the foam reaches 289 °C, recording a net temperature increase
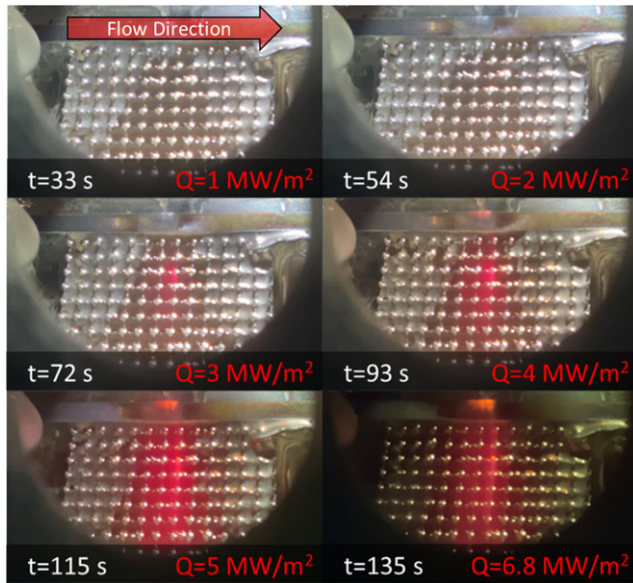
Figure 17. Image series of increasing heat flux from a vantage point focusing on the case A_f foam. The closer viewpoint offers a better view of surface stability in the foams during high heat flux operation. A red lithium ionization glow can be seen over the lithium-filled structures. The bare stainless steel outside of the filled lithium module is also under direct impingement, heating to potentially damaging temperatures while the liquid lithium module remains unharmed.

of 44 °C over 135 s of beam operation with cooling, and a peak-to-trough temperature increase of 62 °C over 90 s of high heat flux operation over 2 MW m^{-2}.

The image series presented in figure 17 illustrates the surface stability in a high heat flux environment. For these beam current ramp tests, additional light was added to the chamber for better video quality, therefore the blue Bremsstrahlung radiation emission from the beam striking the surface is less visible. The effect of the beam heating along the centerline of the flow module is still apparent, with increasing reddish glow due to the emission of excited lithium neutrals transitioning to their ground state. This view from the 2.75-inch viewport directly above the test module highlights the case A_f foam performance during the 6.5 V, 100 A Helmholtz condition beam ramp. The lithium surface is mirror-finish clean in a downward V-shape from the edge of the module toward the top of the images, with a thin impurity layer on the surface of the upstream and downstream regions of the foam. As the magnetic field in these tests is continuously active (deactivating the field defocuses the beam and lowers beam current), TEMHD flow through the device is already present at low speeds due to inherent temperature gradients that form through the module.

As the beam current is turned up and topside heat flux increases, rapid swirling motion is seen in tiny impurity particles in multiple cells of the topside surface of the foam. Surface circulation is also seen in the side channels. There is no observable evidence of diminishing surface stability, dryout propensity, or pileup throughout the heat flux ramp, as the surface tension of the liquid lithium acts in the foam structure to anchor

the surface against dryout. This is true up to the maximum 6.8 MW m^{-2}, which the foam withstands for at least 5 s before the beam heating is decreased. Meanwhile, the stainless-steel module edge with no lithium cover (at the top of the images) is damaged by the extreme heat flux.

At the 2.5 to 3 MW m^{-2} range, approximately 65–75 s into the duration of the test, centerline impurities near the module edge (top of the images) indicate the Z-directed (into and out of the page) dryout and pileup forces are still present but are countered by the flow mixing and capillary action of the foam. Impurities on the upstream side of the heat stripe drop into the lithium as they are entrained in rapid motion just beneath the surface. Between 3 and 4 s later, new impurities are seen coming to the surface on the downstream side of the high heat flux region. This is a rare case of impurity motion below the surface of the lithium, which has not been previously observed in lab scale e-beam testing. This illustrates the stabilizing action of the foam structures against the large volume forces present in that region, and potentially the local temperature change starting to allow impurity dissolution into the bulk. This process is displayed in the images in figure 18. Ultimately, the lithium surface remained stable through this event.

The high heat flux e-beam tests discussed in this section provide the strongest evidence for improvement to TEMHD driven, open surface, liquid lithium PFCs utilizing advanced geometries to stabilize the surface while maintaining the propensity for bulk flow. The operating regime for a LiMIT-style TEMHD system was improved by 127%, from 3 MW m^{-2} to 6.8 MW m^{-2}. In comparison to previous LiMIT-style testing, especially the examples given in section 1.1, the improvement is stark. Dryout and pileup have been observed at <1 MW m^{-2}, with damage to the solid structures common above 3 MW m^{-2}. Furthermore, this level of peak heat flux was sustained for at least 5 s with no evidence of impending dryout, pileup, or material failure, over a span of high heat flux impingement lasting 140 s total. This implies a much higher limit to the heat flux handling capabilities of these foam systems.

Future testing aims to extend this important result to more intense fusion relevant conditions, with the aim to test >10 MW m^{-2} heat fluxes at >1 T magnetic fields. TEMHD drive increases with heat flux and decreases with magnetic field, so as the conditions become more extreme, the concentrated lithium acceleration will be tempered by MHD drag in regions outside of the heat stripe. This could amplify dryout and pileup, so it become increasingly important that the structure in direct impingement maintains a stable lithium surface. Based on the lack of any indication of dryout and impressive surface stability, the foam design is expected to have a larger operating window than tested here. Upgrades to the SLiDE apparatus can improve lab scale testing. The e-beam heat flux will return to its full design basis of 20 MW m^{-2} with excursions approaching 40 MW m^{-2}. The Helmholtz coils can handle currents yielding at least 0.2 T magnetic fields. To realize fully fusion relevant testing with *B*-fields approaching 2 T and particle loading, designs are in progress to include the structured foam and other LiMIT-style systems in a lithium loop system for placement in full-scale fusion devices.
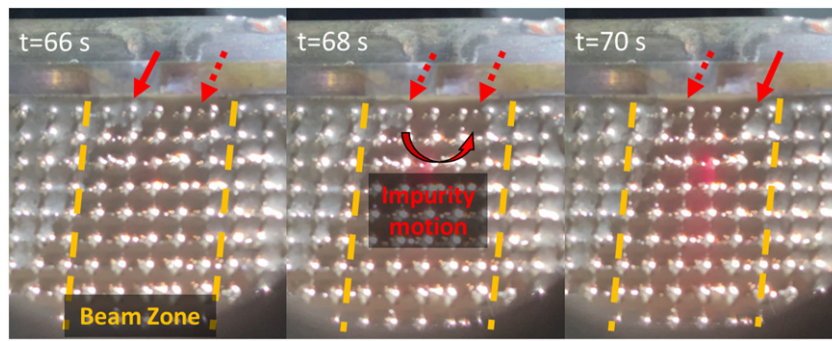
Figure 18. Image series of impurity motion moving under the lithium surface, indicating high dryout forces are present but the lithium surface is stabilized by the foam structures. Solid red arrows indicate impurities are present, dashed red arrows indicate impurities are not present.

4. Conclusion

In this work, the basic LiMIT concept is expanded to include three dimensions of potential flow channels. While TEMHD drive is expected to be lower in these designs due to the smaller structure sizes, the bulk temperature gradients through the structure still work to drive TEMHD in one predominant direction. The foam concept combines the benefits of both LiMIT and CPS systems, enhancing capillary action to stabilize the surface in the face of high heat flux while maintaining steady TEMHD flow with the large pores. Three designs of an ordered cubic structure were modeled and experimentally tested.

Modeling of the foams shows unique development of thermoelectric currents and volume forces due to the thin structures placed in each main axis direction. The Y-directed elements in the gaps between the vertical elements drive the most sustained TEMHD flow in the primary flow direction. Furthermore, the X-directed elements develop current profiles that aid in fighting dryout. Taken together with the flow disruption present due to the 3D structure, the flow profiles that develop are resilient to the dryout effect. The fixed surface models present a conservative velocity profile because of the necessary neglect of surface tension which is expected to improve top surface stability. Accelerated regions of flow under the topside heat flux do not depress and propagate to the extent seen in other LiMIT-style PFC designs. Overall, the foams display lower average flow due to the smaller structures and larger flow channel gaps.

Proof of concept testing experimental testing shows the DMLS 3D printing process creates a robust material that is lithium compatible. The tri-fold foam plate displayed consistent wetting ability and mechanical stability after repeated testing and lithium cleaning cycles. Sustained lithium flow develops through the structures, with the temperature response signifying effective mixing and recirculation of bulk lithium. Velocity magnitudes track numerical modeling of the proof of concept magnetic fields, with some discrepancy due to the lower resolution of the velocimetry setup and the presence of all three foam designs allowing effective decoupling of the surface motion.

High heat flux testing with the SLiDE e-beam expanded the tested viability limit of a LiMIT-style open surface PFC system to 6.8 MW m^{-2}, more than twice as high as the 3 MW m^{-2} failure case observed in Magnum-PSI testing. This value comes from current limits of the e-beam components, not from system failure. The stability of the surface was closely observed in the case A$_f$ foam and no indication of lithium dryout or structural damage in the solid was seen, indicating the dryout mitigation of the foam TEMHD system extends beyond this tested value. Future testing at the University of Illinois will push the limits of the foam system heat tolerance by improving e-beam output. The design is also being scaled and implemented alongside a lithium loop system for testing on fusion relevant devices, in order to further explore the benefits of liquid lithium and prove this PFC concept in reactor relevant magnetic fields over 2 T and divertor heat fluxes beyond 10 MW m^{-2}.

Acknowledgments

ORCID iDs

D.N. Ruzic ⬤ https://orcid.org/0000-0001-9501-1439

References

[1] Lehnen M. *et al* 2015 Disruptions in ITER and strategies for their control and mitigation *J. Nucl. Mater.* **463** 39–48
[2] Raffray A.R. *et al* 2014 The ITER blanket system design challenge *Nucl. Fusion* **54** 033004
[3] Pitts R.A. *et al* 2019 Physics basis for the first ITER tungsten divertor *Nucl. Mater. Energy* **20** 100696
[4] Linke J., Du J., Loewenhoff T., Pintsuk G., Spilker B., Steudel I. and Wirtz M. 2019 Challenges for plasma-facing components in nuclear fusion *Matter Radiat. Extremes* **4** 056201
[5] Ueda Y. *et al* 2017 Baseline high heat flux and plasma facing materials for fusion *Nucl. Fusion* **57** 092006
[6] Coenen J.W. *et al* 2013 Evolution of surface melt damage, its influence on plasma performance and prospects of recovery *J. Nucl. Mater.* **438** S27

[7] Baldwin M.J. and Doerner R.P. 2010 Formation of helium induced nanostructure 'fuzz' on various tungsten grades *J. Nucl. Mater.* **404** 165

[8] Wright G.M. *et al* 2013 Comparison of tungsten nano-tendrils grown in Alcator C-Mod and linear plasma devices *J. Nucl. Mater.* **438** S84

[9] Mansfield D.K. *et al* 2001 Observations concerning the injection of a lithium aerosol into the edge of TFTR discharges *Nucl. Fusion* **41** 1823–34

[10] Tuccillo A.A. *et al* 2009 Overview of the FTU results *Nucl. Fusion* **49** 104013

[11] Majeski R. *et al* 2003 CDX-U operation with a large area liquid lithium limiter *J. Nucl. Mater.* **313–316** 625–9

[12] Majeski R. *et al* 2005 Recent liquid lithium limiter experiments in CDX-U *Nucl. Fusion* **45** 519–23

[13] Schmitt J.C. *et al* 2015 High performance discharges in the lithium tokamak experiment with liquid lithium walls *Phys. Plasmas* **22** 056112

[14] Maingi R. *et al* 2012 The effect of progressively increasing lithium coatings on plasma discharge characteristics, transport, edge profiles and ELM stability in the national spherical torus experiment *Nucl. Fusion* **52** 083001

[15] De Castro A., Moynihan C., Stemmley S., Szott M. and Ruzic D.N. 2021 Lithium, a path to make fusion energy affordable *Phys. Plasmas* **28** 050901

[16] Shercliff J.A. 1979 Thermoelectric magnetohydrodynamics *J. Fluid Mech.* **91** 231–51

[17] Jaworski M.A. 2009 Thermoelectric Magnetohydrodynamic and Thermocapillary Driven Flows of Liquid Conductors in Magnetic Fields (University of Illinois at Urbana-Champaign)

[18] Ruzic D.N., Xu W., Andruczyk D. and Jaworski M.A. 2011 Lithium-metal infused trenches (LiMIT) for heat removal in fusion devices *Nucl. Fusion* **51** 102002

[19] Xu W., Curreli D., Andruczyk D., Mui T., Switts R. and Ruzic D.N. 2013 Heat transfer of TEMHD driven lithium flow in stainless steel trenches *J. Nucl. Mater.* **438** S422

[20] Xu W., Curreli D. and Ruzic D.N. 2014 Computational studies of thermoelectric MHD driven liquid lithium flow in metal trenches *Fusion Eng. Des.* **89** 2868–74

[21] Xu W. *et al* 2015 Vertical flow in the thermoelectric liquid metal plasma facing structures (TELS) facility at Illinois *J. Nucl. Mater.* **463** 1181–5

[22] Hu J.S., Ren J., Sun Z., Zuo G.Z., Yang Q.X., Li J.G., Mansfield D.K., Zakharov L.E. and Ruzic D.N. 2014 An overview of lithium experiments on HT-7 and EAST during 2012 *Fusion Eng. Des.* **89** 2875–85

[23] Zuo G.Z., Ren J., Hu J.S., Sun Z., Yang Q.X., Li J.G., Zakharov L.E. and Ruzic D.N. 2014 Liquid lithium surface control and

its effect on plasma performance in the HT-7 tokamak *Fusion Eng. Des.* **89** 2845–52

[24] Ren J., Zuo G.Z., Hu J.S., Sun Z., Li J.G., Zakharov L.E., Ruzic D.N. and Xu W.Y. 2016 Investigations on interactions between the flowing liquid lithium limiter and plasmas *Fusion Eng. Des.* **102** 36–43

[25] Fiflis P., Morgan T.W., Brons S., Van Eden G.G., Van Den Berg M.A., Xu W., Curreli D. and Ruzic D.N. 2015 Performance of the lithium metal infused trenches in the magnum PSI linear plasma simulator *Nucl. Fusion* **55** 113004

[26] Szott M. and Ruzic D.N. 2020 2D moving mesh modeling of lithium dryout in open surface liquid metal flow applications *Fusion Eng. Des.* **154** 111512

[27] Fiflis P., Christenson M., Szott M., Kalathiparambil K. and Ruzic D.N. 2016 Free surface stability of liquid metal plasma facing components *Nucl. Fusion* **56** 106020

[28] Szott M., Fiflis P., Kalathiparambil K., Shchelkanov I., Ruzic D.N., Jurczyk B., Stubbers R. and Foster C.J. 2015 Wetting of lithium on nanostructured surfaces for first wall components *Proc. Symp. Fusion Engineering* vol 2016 (Austin, Texas, 31 May–4 June 2015) (http://ece-events.unm.edu/ppcsofe2015/)

[29] Hammouti S., Holybee B., Christenson M., Szott M., Kalathiparambil K., Stemmley S., Jurczyk B. and Ruzic D.N. 2018 Wetting of liquid lithium on fusion-relevant materials microtextured by femtosecond laser exposure *J. Nucl. Mater.* **508** 237–48

[30] Szott M. 2016 MSc Thesis *Flow Control and Associated Technologies to Advance the Application of TEMHD-Driven Liquid Lithium in Fusion Devices* (University of Illinois)

[31] Christenson M. 2018 The design and development of hydrogen isotope extraction technologies for a LiMIT-style liquid lithium loop *PhD Thesis* University of Illinois

[32] Christenson M., Moynihan C. and Ruzic D.N. 2018 A distillation column for hydrogen isotope removal from liquid lithium *Fusion Eng. Des.* **135** 81–7

[33] Krasheninnikov S.I., Zakharov L.E. and Pereverzev G.V. 2003 On lithium walls and the performance of magnetic fusion devices *Phys. Plasmas* **10** 1678–82

[34] Xu W. 2015 Experimental and numerical analysis of thermo-electric magnetohydrodynamic driven liquid lithium flow in open channels for fusion applications *PhD Thesis* University of Illinois

[35] COMSOL Multiphysics 2019 COMSOL multiphysics reference manual *(version 5.4)* (www.comsol.com)

[36] Schindelin J. *et al* 2012 Fiji: an open-source platform for biological-image analysis *Nat. Methods* **9** 676–82

[37] FFmpeg Developers 2020 *Ff. Developers FFmpeg* (http://ffmpeg.org)